Nano Research
2023, 16(1): 1491–1499

ISSN 1998-0124 CN 11-5974/O4
https://doi.org/10.1007/s12274-022-4693-8

Research Article

Excitation orthogonalized upconversion nanoprobe for instant visual detection of trinitrotoluene

Xu Li[1], Xu Zhao[1], Xiaoyu Xu[2], Yang Lu[1], Jiahang Wu[1], Fangmeng Liu[1], Xu Yan[1], Peng Sun[1], Chenguang Wang[1], Xianggui Kong[3], Xiaomin Liu[1] (✉), and Geyu Lu[1] (✉)

[1] *State Key Laboratory of Integrated Optoelectronics, College of Electronic Science and Engineering, Jilin University, Changchun 130012, China*
[2] *Department of Public Security of Jilin Province, Changchun 130051, China*
[3] *State Key Laboratory of Luminescence and Applications, Changchun Institute of Optics, Fine Mechanics and physics, Chinese Academy of Science, Changchun 130033, China*

Received: 24 April 2022 / **Revised:** 5 June 2022 / **Accepted:** 22 June 2022

ABSTRACT

Excitation-emission orthogonalized luminescent upconversion nanoparticles (OUCNPs), which can respond to changes in external stimuli accordingly, show great promise in many intelligent applications. However, the construction of such materials mostly relies on the selective absorption of Nd^{3+} and Yb^{3+} at different wavelengths and the long-range energy migration between the layers, resulting in complex structures and limited orthogonal luminescence intensity. Herein, we developed a relatively simple structure of OUCNPs (β-$NaErF_4$@$NaLuF_4$@$NaYF_4$:20%Yb, 2%Er@$NaLuF_4$), where the fluorescence emission switches from red to green when the excitation wavelength is shifted from 808 to 980 nm. This structure exhibits high-quality, independent, and non-interfering orthogonal luminescence properties without Nd^{3+} sensitization and long-range energy migration. As a proof of concept, we demonstrate the application of the designed OUCNPs in anti-counterfeiting. We also prepared OUCNPs@PEI (PEI = polyethylenimine) self-referencing fluorescent probes to enable quantitative analysis of trinitrotoluene (TNT) in solution with a detection limit of 3.04 μM. The probes can be made into test strips for portable on-site visual detection of TNT, and can also be used to image latent fingerprints and detect explosive residues in fingerprints simultaneously. The concept proposed in this work can be extended to the visual detection of a larger range of organic and biological molecules, and is highly promising for practical applications.

KEYWORDS

orthogonal luminescence, $NaErF_4$, core/multi-shell structure, anti-counterfeiting, trinitrotoluene (TNT) detection

1 Introduction

With the rapid development of nanoscience and nanotechnology, the design of various stimulus-responsive nanoprobes for display [1–3], information storage [4–6], chemical sensing [7–9], biomedical [10–12], and other applications has attracted a lot of attention and interest. Light is known to be more advantageous than many other stimuli such as electromagnetic fields, temperature, pH, and chemical reactions because of its precision, remoteness, and spatiotemporal controllability in different environments [3, 11, 13–16]. Photon upconversion is a powerful means of converting low-energy photons to high-energy photons (e.g., from near-infrared (NIR) to visible light emission). As an ideal candidate for upconversion (UC), lanthanide ions have a unique electronic configuration with a rich step-like energy level structure that enables them to produce a wide range of UC emission spectra under NIR excitation, covering the ultraviolet, visible, and NIR spectral regions [17]. The UC emissions have large anti-Stokes shifts, narrow emission bands, long fluorescence lifetimes, good photochemical stability, and low autofluorescence [18–23]. In particular, based on the property that 808 and 980 nm can excite sensitizer ions Nd^{3+} and Yb^{3+}, respectively, excitation-emission orthogonal response type of UC luminescence has been recently achieved in some special designed nanostructures [24–26]. Orthogonal luminescence, which can give a corresponding response to changes in the external stimuli, whereas conventional UC materials only give a single response under fixed wavelength excitation, further promotes intelligent applications of lanthanide materials, such as rewritable optical memory [4], imaging-guided on-demand therapy [27–29], etc.

In the design of orthogonal luminescent upconversion nanoparticles (OUCNPs), different types of activator ions are usually distributed in different spatial regions within the nanoparticle through a core/multi-shell structure. The selective absorption and energy migration of 808 and 980 nm by the sensitizer ions Nd^{3+} and Yb^{3+} enables the excitation of different activator ions by switching the external excitation source, and their luminescence is independent of each other. For example, Yan et al. [30] designed a novel OUCNPs ($NaGdF_4$:Yb^{3+}/Er^{3+}@$NaYF_4$@$NaYF_4$:Yb^{3+}/Tm^{3+}@$NaYbF_4$:Nd^{3+}@$NaYF_4$) that exhibit UV and green UC emission by adjusting the 808 and 980 nm excitation respectively, for reversible handedness inversion. In 2021, Hong et al. [2] developed an OUCNPs with core/sextuple-shell structure ($LiYbF_4$: Tm@$LiGdF_4$@$LiGdF_4$:Yb, Er@$LiYF_4$:Nd, Yb@$LiGdF_4$@

Address correspondence to Xiaomin Liu, xiaominliu@jlu.edu.cn; Geyu Lu, lugy@jlu.edu.cn

$LiErF_4$:Tm@$LiGdF_4$), which emits green, blue, and red light under 808, 980, and 1,532 nm excitations, respectively. It is obvious that most OUCNPs are limited to Nd^{3+} and Yb^{3+} co-sensitive materials with complex structures because they require different doping and luminescence modes in different spatial regions. And the necessary long-range energy migration processes between the multi-layers inevitably cause the loss of excitation energy, resulting in the decrease of orthogonal luminescence intensity. Therefore, the development of OUCNPs with high luminescence quality and less complex structure remains a challenge.

In this work, based on the unique property that $NaErF_4$@$NaYF_4$ (or $NaLuF_4$, $NaGdF_4$ shells, etc.) can be excited at multiple NIR wavelengths (800, 980, and 1,530 nm), emitting near-monochromatic red light as reported by our group previously [31], we developed a relatively simple structure of OUCNPs: β-$NaErF_4$@$NaLuF_4$@$NaYF_4$:20%Yb, 2%Er@$NaLuF_4$ (C/S1/S2/S3). $NaErF_4$@$NaLuF_4$ was used as the red light region, on which a second $NaYF_4$:20%Yb, 2%Er shell, and a third inert shell of $NaLuF_4$ were epitaxially grown as the green light region. The high-quality orthogonal luminescence properties of the designed OUCNPs can be obtained only by simply regulating the thickness of the inert shell S1 ($NaLuF_4$) to avoid the diffusion of Er^{3+} ions from the $NaErF_4$ core to the S2 ($NaYF_4$:20%Yb, 2%Er) shell: The monochromatic red emission occurs upon 808 nm excitation, whereas the strong green emission appears upon 980 nm excitation. Compared with the previously reported OUCNPs, our design (i) achieves 808 nm excitation without Nd^{3+} ions and has only one doping layer, which avoids the complex doping patterns and simplifies the synthesis; (ii) does not require any layers for long-range energy migration, and the excitation energy is all confined to the luminescent functional region, which can effectively reduce the energy loss. As a proof-of-principle, we demonstrate the application of the designed OUCNPs for anti-counterfeiting and self-referential instant visual detection of trinitrotoluene (TNT) .

2 Materials and methods

2.1 Materials

$ErCl_3·6H_2O$ (99.9%), oleylamine (OM, 70%), 1-octadecene (ODE, 90%), oleic acid (OA, 90%), and CF_3COONa were purchased from Sigma-Aldrich. Ln_2O_3 (Ln: Y, Yb, Lu, and Er), trifluoroacetic acid (CF_3COOH, >99.5%), polyethyleneimine (PEI), sodium hydroxide (NaOH), and ammonium fluoride (NH_4F) were purchased from Aladdin. Absolute ethyl alcohol, acetone, methanol, and cyclohexane were purchased from Xilong Scientific. Benzophenone (BP), p-nitroaniline (p-NA), o-nitroaniline (o-NA), benzoquinone (BQ), chloranil (CA), p-nitrobenzaldehyde (p-NBA), and nitrobenzene (NB) were purchased from Sigma-Aldrich. All the above chemicals were used directly without further purification. TNT were purchased from MACKLIN and recrystallized with ethanol before use.

2.2 Synthesis of the $NaErF_4$ core nanoparticles

1.0 mmol $ErCl_3·6H_2O$, 15 mL ODE, and 6 mL OA were added into a 50 mL three-neck flask. Nitrogen was passed into the three-neck flask for 30 min to expel air, and then the mixture was heated to 160 °C and stirred for 35 min. At that moment, the solid component in the three-neck flask was completely dissolved and the solution was transparent, which indicated the successful coordination of rare earth ions with oleic acid molecules. The mixture was cooled naturally to below 50 °C. Then a solution of 8 mL methanol mixed up with NaOH (2.5 mmol) and NH_4F (4 mmol) was added and heated to 75 °C for 30 min to remove the superfluous methanol. Next, the solution was gradually heated to 300 °C and stirred continuously for 90 min. After cooling the solution to room temperature, it was washed once with acetone and then twice with ethanol. Each centrifugation was 6 min (6,000 r/min). And then, the core $NaErF_4$ nanoparticles were obtained and dispersed in 8 mL of cyclohexane. The whole process was carried out under N_2 protection.

2.3 Synthesis of trifluoroacetate salt

First, 2 mmol of Ln_2O_3 (Ln: Y, Yb, Lu, and Er) and 12 mL of deionized water were poured into a 50 mL single-necked flask, and 12 mL of trifluoroacetic acid was added while stirring. The solution was condensed and refluxed at 95 °C with stirring until clarified. A transparent solution was obtained after the reaction. Excess water and trifluoroacetic acid were removed by rotary evaporation at 65 °C. Finally, the obtained solid was dried and powdered to obtain the corresponding trifluoroacetate salt, denoted as $(CF_3COO)_3Ln·3H_2O$.

2.4 Synthesis of $NaLuF_4$ precursor

$CF_3COONa·3H_2O$ (4 mmol), $(CF_3COO)_3Lu·3H_2O$ (4 mmol), oleic acid (12 mL), oleylamine (12 mL), and 1-octadecene (20 mL) were added into a 100 mL three-neck flask and heated to 120 °C in a vacuum for 35 min to remove oxygen and water. Afterwards, the solution was heated to 290 °C for 45 min and then cooled down to room temperature. The final product was washed with ethanol and dispersed in ODE (10 mL) for later use.

2.5 Synthesis of $NaYF_4$:20%Yb, 2%Er precursor

$(CF_3COO)_3Y·3H_2O$ (3.12 mmol), $(CF_3COO)_3Yb·3H_2O$ (0.8 mmol), $(CF_3COO)_3Er·3H_2O$ (0.08 mmol), $CF_3COONa·3H_2O$ (4 mmol), oleic acid (12 mL), oleylamine (12 mL), and 1-octadecene (20 mL) were added into a 100 mL three-neck flask and heated to 120 °C in a vacuum for 35 min to remove oxygen and water. Afterwards, the solution was heated to 290 °C for 45 min and then cooled down to room temperature. The final product was washed with ethanol and dispersed in ODE (10 mL) for later use.

2.6 Synthesis of C/S1/S2/S3 OUCNPs

Firstly, $NaErF_4$ cyclohexane solution (2 mL) was added into a 50 mL three-necked flask with oleic acid (6 mL) and 1-octadecene (15 mL). The solution was heated to 85 °C and kept for 30 min to remove the cyclohexane solvent. Then, the solution was heated to 300 °C, and $NaLuF_4$ (0.75 mmol) precursor was injected into the flask in two equal fractions at 30 min intervals. Then, $NaYF_4$:20%Yb, 2%Er (1 mmol) precursor was injected into the flask in two equal fractions at 30 min intervals. Lastly, $NaLuF_4$ (1.5 mmol) was also injected in three equal fractions at 30 min intervals. It was maintained for another 1 h at 300 °C after the last injection and then reduced to room temperature. Finally, the cooling solution was washed by acetone and ethanol, respectively, and dispersed in cyclohexane (4 mL).

2.7 Synthesis of C/S1/S2/S3 OUCNPs with different S1 shell thicknesses

The synthesis method is the same as that described above for $NaErF_4$@$NaLuF_4$@$NaYF_4$:20%Yb, 2%Er@$NaLuF_4$, with the difference only in the amount of shell precursors injected during the coating of the S1 shell layer. We just adjusted C:S1:S2:S3 to 1:1:4:6, 1:2:4:6, and 1:3:4:6 for preparing the target products in each reaction.

2.8 Anti-counterfeiting application

As a display of the anti-counterfeiting function, only relatively simple operations are required. By pre-designing the pattern, we applied the prepared oil-phase material as ink directly to the white paper. $NaErF_4$@$NaLuF_4$ and $NaErF_4$@$NaLuF_4$@$NaYF_4$:20%Yb, 2%Er@$NaLuF_4$ were applied in different areas. Then the patterns were irradiated with 808 and 980 nm lasers respectively, and photographed with an Apple phone in a dark environment for better results.

2.9 Preparation of PEI modified OUCNPs

Oleic acid molecules attached to the surface of nanoparticles prepared by previous solvothermal methods. It has been reported in the literature that surface oleic acid molecules can be removed by using hydrochloric acid protonation. 4 mL HCl (PH = 4) was added into a 20 mL glass bottle with 2 mL cyclohexane and 2 mL of cyclohexane containing OUCNPs, and the mixture was stirred vigorously for 12 h. At this time, the nanoparticles have been transferred from cyclohexane to the lower aqueous hydrochloric acid solution. The lower solution was extracted and centrifuged to obtain hydrophilic OUCNPs@free. Finally, the OUCNPs@free were dispersed in 4 mL deionized water. Next, 200 mg of polyethyleneimine was dissolved in 10 mL of deionized water, from which 2 mL was removed and mixed with 2 mL of OUCNPs@free as described above. The mixture stirred overnight was washed and centrifuged to remove excess PEI. The PEI-modified upconversion nanoparticles (OUCNPs@PEI) were obtained dispersed in 4 mL of deionized water. Repeat the above operation to prepare another portion of OUCNPs@PEI, disperse it in 4 mL of acetonitrile and set aside.

2.10 TNT detection in solution

First, the eight analytes, p-NA, o-NA, BQ, CA, p-NBA, NB, BP, and TNT, were prepared as a solution of acetonitrile at a certain concentration. Dissolve 200 mg of PEI in 10 mL of acetonitrile solution and take out 8 portions to mix with various analytes separately. A certain amount of acetonitrile was added so that the final volume was 4 mL and the final concentration of analytes was the same. The absorption spectra of the eight analytes and eight mixtures were measured by UV-2550 spectrophotometer (Shimadzu, Japan). The above procedure was repeated, except that instead of PEI solution, 40 μL of OUCNPs@PEI acetonitrile solution of known concentration was added, and then their fluorescence emission spectra were measured by the Ocean Optics QE Pro (a high-performance spectrometer) under 980 nm excitation. Finally, the spectral responses of OUCNPs@PEI after the addition of different concentrations of TNT were measured at 808 and 980 nm excitations, respectively.

2.11 Preparation of test strips and *in situ* instant detection of TNT powder

We made the TNT detection test strips by immersing the cut strips into OUCNPs@PEI aqueous solution for about 10 min to adsorb the OUCNPs@PEI into the filter paper due to hydrophilic and hydrogen bonding interactions, and then removing them and placing them in a dark place to dry naturally. It was repeated several times to obtain a batch of the same TNT test strips. Different concentrations of TNT (0, 5, 15, 20, 25, 30, 50, 60, 70, 80, 90, 100, 200, 400, 1,000, 2,000, 3,000, and 4,000 μM) acetonitrile solutions were dropped on the solid surface, dried, and scraped with the test strips just prepared. The color of the test strips changed from green to yellow to red with increasing TNT concentration under 980 nm excitation. While under 808 nm, they showed red luminescence and no obvious difference in naked eye observation.

2.12 *In situ* instant detection of TNT powder and imaging of latent fingerprint

The volunteer's finger was first cleaned; a certain concentration of TNT solution was placed on the fingertip, and then the fingertip was pressed on a clean glass slice to collect fingerprints. The operation was repeated to obtain fingerprints with different amounts of TNT. These glass pieces were then immersed in the solution of OUCNPs@PEI for about 10 min and removed to dry. The samples were irradiated with 808 and 980 nm lasers in a dark environment, while pictures were taken with an Apple phone. Under 980 nm excitation, the fingerprints showed a gradient from green to red with increasing TNT concentration. While under 808 nm excitation, the fingerprints were red. It should be noted that the fingerprint pattern obtained was relatively clear.

3 Results and discussion

3.1 Design and characterization of OUCNPs

Figure 1(a) shows a schematic diagram of the structure and composition of the designed $NaErF_4$@$NaLuF_4$@$NaYF_4$:20%Yb, 2%Er@$NaLuF_4$ (C/S1/S2/S3) OUCNPs, which were synthesized by a one-pot continuous layer-by-layer Ostwald ripening method [32]. Since small particles with a large surface-to-volume ratio are energetically more unstable in the colloidal system, small particles dissolve and then deposit on the surface of large particles, generating nanoparticles with a core–shell structure. Each layer has a unique composition, controllable thickness, and exclusive features, which together constitute this orthogonal excitation-emission characteristic. $NaErF_4$ was used as the core material, and the bare core nanoparticles were not luminescent due to the surface defects and concentration quenching. After passivation of surface defects by epitaxially coating the inert shell $NaLuF_4$ (S1), near-monochromatic red UC emission under excitation at multiple wavelengths (808, 980, and 1,530 nm) can be obtained based on the step-like energy level characteristics of Er^{3+}, and the concentration quenching is effectively suppressed [31, 33, 34]. This lays the foundation for the development of high-quality and less

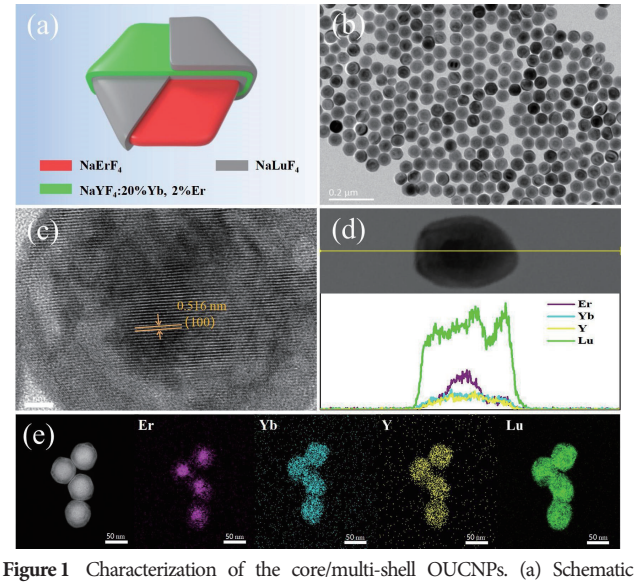

Figure 1 Characterization of the core/multi-shell OUCNPs. (a) Schematic representation of the core/multi-shell structure of OUCNPs. (b) The TEM image of the $NaErF_4$@$NaLuF_4$@$NaYF_4$:Yb, Er@$NaLuF_4$ nanoparticles. (c) HRTEM image of OUCNPs with a lattice distance of 0.516 nm. Scale bar is 5 nm. (d) TEM image and corresponding EDS of Er^{3+}, Yb^{3+}, Y^{3+}, and Lu^{3+} ions of the nanoparticle. (e) HAADF image and corresponding elemental mapping of Er^{3+}, Yb^{3+}, Y^{3+}, and Lu^{3+} of OUCNPs. Scale bar is 50 nm.

complex orthogonal upconversion nanostructures. Another excitation-responsive luminescence mode is achieved by the S2 ($NaYF_4$:20%Yb, 2%Er) shell, which exhibits strong green UC emission only triggered by 980 nm due to the presence of Yb^{3+} ions. S1 ($NaLuF_4$) is an undoped inert shell that acts on the one hand to passivate the surface of the core in order to maintain the near-monochromatic red UC emission under 808 nm excitation. On the other hand, it acts as a buffer layer to avoid the diffusion of Er^{3+} from the core into the S2 layer, which generates a concentration quenching and leads to a reduction of the green UC emission. To enhance the overall UC luminescence, we coated the outermost layer with an inert shell $NaLuF_4$ (S3) to passivate the surface defects. Consequently, the designed OUCNPs obtain independent and orthogonal excitation-emission characteristic, with near-monochromatic red UC emission from the core under 808 nm excitation and green UC emission from the S2 layer under 980 nm excitation.

The $NaErF_4$ core nanoparticles show an approximate hexagonal shape with a uniform distribution and an average size of ~ 32 nm (Fig. S1 in the Electronic Supplementary Material (ESM)). Following the successive epitaxial growth of three different shells (S1: $NaLuF_4$, S2: $NaYF_4$: Yb/Er, and S3: $NaLuF_4$), the final products were collected and dispersed in cyclohexane. After coating these three shells, the OUCNPs still maintained hexagon morphology. The transmission electron microscopy (TEM) picture of the OUCNPs shows homogenous core/multi-shell nanoparticles having a narrow size distribution and an average size of 56.4 nm (Fig. 1(b) and Fig. S2 in the ESM). Each shell has a thickness of around 3.5, 4.6, and 4.1 nm, respectively (Fig. S3 in the ESM). Figure 1(c) exhibits a high-resolution transmission electron microscopy (HRTEM) image, and clear lattice stripes can be seen with a lattice spacing of 0.516 nm, which corresponds to the (100) crystal plane of a standard hexagonal-phase $NaErF_4$ nanocrystal. Furthermore, the power X-ray diffraction (XRD) patterns of the core and OUCNPs in Fig. S4 in the ESM are in good accordance with the hexagonal phase of $NaErF_4$ nanocrystal without any significant impurity phases, suggesting that all nanoparticles have a hexagonal structure. The increase in size provides preliminary evidence of the formation of core/multi-shell nanostructure, and the distribution of each lanthanide element is further evidence of the successful synthesis of the OUCNPs. Figure 1(d) depicts the elemental profiles of Er^{3+}, Yb^{3+}, Y^{3+}, and Lu^{3+} ions from scanning transmission electron microscopy (STEM), indicating that Er^{3+} ions are mostly localized in the middle while Lu^{3+} ions are distributed at the ends of OUCNPs. Moreover, the core/multi-shell structure of OUCNPs is also confirmed by the high-angle annular dark field scanning transmission electron microscopy (HAADF-STEM) image shown in Fig. 1(e), as it can better distinguish the heavier lanthanides (Er and Lu, the brighter part) from the lighter elements (Y, the darker part) in the nanoparticles. The corresponding HAADF-STEM-energy dispersive spectrometer (EDS) mapping images and the energy dispersive X-ray spectroscopy (EDX) spectrum (Fig. S5 in the ESM) also reaffirm the distributions of lanthanide ions in such OUCNPs, in agreement with the results of Fig. 1(d), further validating the nanoparticle composition and the success of the synthesis.

3.2 Orthogonal emissive performance of OUCNPs

To confirm our hypothesis, we investigated the emission characteristics of the as-prepared $NaErF_4$@$NaLuF_4$@$NaYF_4$:20%Yb, 2%Er@$NaLuF_4$ OUCNPs by altering the excitation wavelength. The nanoparticles display apparent excitation wavelength-dependent spectral characteristics, shown in Fig. 2(a). Figure S6 in the ESM shows the emission spectrum of OUCNPs under excitation at 1,530 nm. At 808 nm excitation, only the monochromatic red UC emission from the core-S1 fraction ($NaErF_4$@$NaLuF_4$) occurs in the ultraviolet–visible (UV–vis) region. Only under excitation at 980 nm, strong green UC emission from S2-S3 fraction ($NaYF_4$:20%Yb, 2%Er@$NaLuF_4$) appears, and it should be noted that the UC red emission from the core is still present under excitation at 980 nm due to the multi-wavelength excitable nature of $NaErF_4$@$NaLuF_4$. Figure 2(b) illustrates the energy transfer paths of OUCNPs under 808 and 980 nm excitation, respectively. In the core-S1 fraction, the high concentration of Er^{3+} ions in the core plays a role as a sensitizer in addition to being an activator. The high concentration will increase the cross-relaxation between Er^{3+} ions (CR_{808ex}: $^2I_{9/2} \rightarrow {}^4S_{3/2} + {}^4I_{13/2}$ and $^4S_{3/2} + {}^4I_{9/2} \rightarrow {}^2F_{9/2}$), resulting in an increase in the population of the $^4F_{9/2}$ energy level and obtaining strong monochromatic red UC emission. In the S2-S3 part, the Yb^{3+} sensitizer only absorbs the excitation light from 980 nm and transfers the obtained energy to the neighboring Er^{3+} activator. As shown in Fig. 2(b), under excitation at 980 nm, the $^4I_{11/2}$ energy level of Er^{3+} ions can be efficiently filled by energy transfer from Yb^{3+} to Er^{3+} ions. The $^4F_{7/2}$, $^2H_{11/2}$, and $^4S_{3/2}$ energy levels of Er^{3+} ions become highly populated through energy transfer UC processes, resulting in the release of strong green UC emission. These luminescence photos inserted in Fig. 2(a) validate the distinct emissions from the OUCNPs when the excitation wavelength is changed. The cyclohexane solution of these nanoparticles exhibits a transition from red to green when switching from 808 to 980 nm irradiation, indicating the orthogonal excitation–emission property. This spectral difference

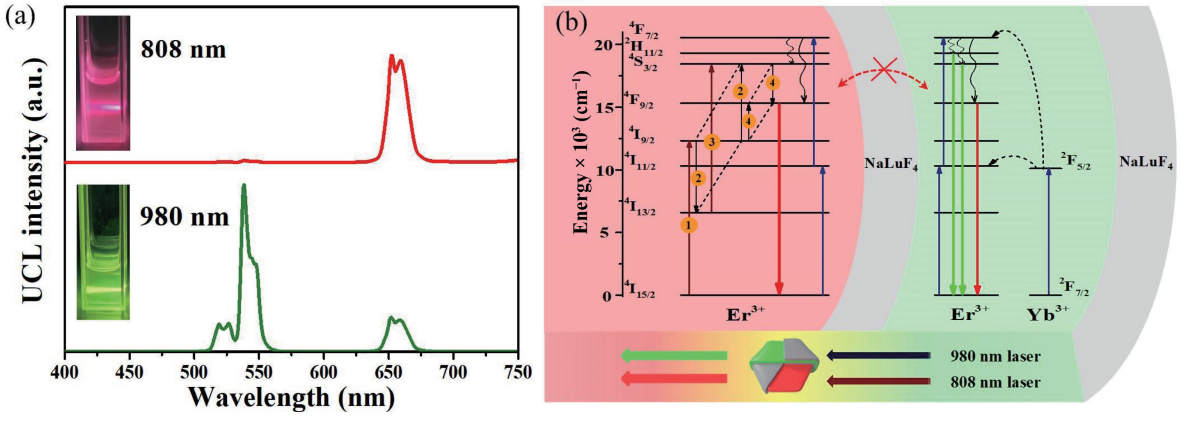

Figure 2 (a) Upconversion luminescence spectra of OUCNPs upon excitation with 808 nm (0.5 W/cm²) and 980 nm (0.5 W/cm²) laser, respectively. The insets show the corresponding digital photograph of upconverting luminescence from the OUCNPs in cyclohexane. (b) Illustration of the OUCNPs' energy level diagrams under 808 and 980 nm laser excitations, respectively.

responds to the fact that the energy transfer modes of the two luminescent regions are different and do not interfere with each other, which is consistent with the expected mechanism.

3.3 Structure optimization of OUCNPs

As mentioned earlier, the structure can be divided into two regions, namely, the $NaErF_4$@$NaLuF_4$ Core-S1 red emission part and the $NaYF_4$:20%Yb, 2%Er@$NaLuF_4$ S2-S3 green emission part. The presence of the S1 ($NaLuF_4$) layer can prevent ion diffusion and energy transfer between the two luminescent regions and facilitates the acquisition of the respective strong UC emission. The thickness of the filtration S1 layer is critical for controlling the emission. As shown in Fig. S7(a) in the ESM, when the S1 layer is thin ($NaErF_4$:$NaLuF_4$ = 1:1), Er^{3+} ions in the core diffuse along the concentration gradient toward the S2 layer, and this diffusion effect is unavoidable in the high-temperature synthesis, leading to the weakened green UC emission in the S2 ($NaYF_4$:20%Yb, 2%Er) layer due to the concentration quenching. As the thickness of S1 layer increases, the green UC emission gradually enhances and the red to green ratio decreases significantly ($NaErF_4$:$NaLuF_4$ = 1:3), indicating that a sufficiently thick layer can effectively avoid ion diffusion and obtain a strong green UC light under 980 nm excitation. In contrast, although the red emission is also slightly enhanced with the increase of S1 layer thickness under 808 nm excitation (Fig. S7(b) in the ESM), it is not as pronounced as the enhancement of green emission under 980 nm excitation. This is due to the protection of the $NaErF_4$ core by the two inert shells (S1 and S3), which makes the diffusion of Er^{3+} ions from the core to the S2 layer insignificant for the red UC emission of $NaErF_4$. Thus, the optimal ratio for these $NaErF_4$@$NaLuF_4$@$NaYF_4$:20%Yb, 2%Er@$NaLuF_4$ OUCNPs is 1:3:4:6. Compared with some reported OUCNPs (Table S1 in the ESM), our design (1) achieves 808 nm excitation in the absence of Nd^{3+}, avoiding multilayer complex doping patterns and simplifying the synthesis; (2) has no long-range modulated energy migration processes, and the excitation energy is all confined to the luminescent functional region, which can effectively reduce the energy loss; (3) localizes two different luminescence modes in the same nanoparticle, separated in different substructures by an inert shell, achieving their respective functions without interfering with each other.

3.4 Application of OUCNPs in anti-counterfeiting

Taking advantage of the significant orthogonal excitation-emission property, a multi-dimensional logo was designed using the OUCNPs (Fig. 3). Multi-dimensional here means having different luminescence and displaying different patterns at different wavelengths [26, 31, 35–37]. The synthesized OUCNPs, uniformly dispersed in cyclohexane, are used as ink and applied directly to the paper according to a pre-designed pattern. In daylight, the various patterns on the paper are in invisible. Under 808 nm excitation, all patterns coated with ink appear red, and only the outline of the pattern can be recognized without distinguishing between patterns with the same shape. In contrast, under 980 nm excitation, the area of $NaErF_4$@$NaLuF_4$ (C/S1) still shows red while the area of $NaYF_4$:20%Yb, 2%Er@$NaLuF_4$ (S2/S3) shows green, and each pattern can be clearly distinguished, which greatly improves the anti-counterfeiting performance and proves their potential application.

3.5 Application of OUCNPs in TNT detection

As an application-based demonstration, we also investigated the use of OUCNPs for self-referential instant visual detection of TNT accompanied by fingerprint imaging. Since its invention in the 19th century, TNT has been commonly used as an explosive in military and warfare, which inevitably resulted in soil and water pollution, toxicity to organisms, and pathogenicity [38]. In addition to these problems, TNT, as an explosive, is often used by terrorists in terrorist attacks, posing a serious threat to national defense and public safety [39]. On-site detection of trace amounts of TNT deposited on surfaces can meet the homeland security needs of public places such as parcel sorting centers and passenger transportation centers [40, 41]. Current approaches for detecting TNT residues on solid surfaces (e.g., ion mobility spectrometry, gas/liquid chromatography) are often off-site and require vapor sample and pre-concentration with complicated and expensive instruments, making them unsuitable for most on-site identifications [42–44]. Therefore, the development of portable, visual, and easy-to-operate sensitive detection techniques remains a challenging. The as-designed OUCNPs probe is promising to meet this challenge.

We constructed the PEI functionalized orthogonal luminescent sensing probe as a specific recognition element for TNT. The detection principle is that the electron-absorbing analyte TNT readily reacts with the electron-giving amino group on PEI to form a Meisenheimer complex [45, 46]. This complex has a broad and strong absorption around 500 nm and can selectively quench

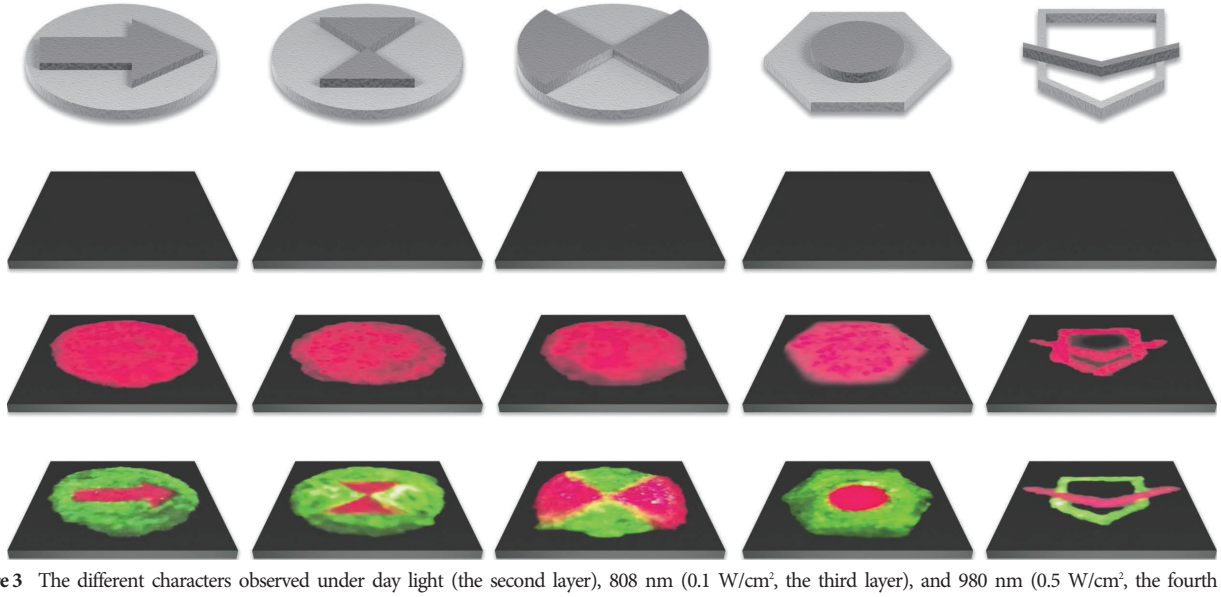

Figure 3 The different characters observed under day light (the second layer), 808 nm (0.1 W/cm^2, the third layer), and 980 nm (0.5 W/cm^2, the fourth layer) excitation, respectively.

the green UC emission of OUCNPs excited at 980 nm, but has almost no effect on the red light under 808 nm excitation, thus enabling the self-referential detection of TNT (Fig. 4(a)). In addition, the reduction of the green emission of the probe leads to a visible color change, which facilitates the visual detection of TNT. Before that, due to the presence of hydrophobic ligand OA on the surface of OUCNPs, we need to transfer the oil phase material to the aqueous phase. As reported in the literature, the oleic acid ligands are protonated by hydrochloric acid to detach them from the surface of the OUCNPs [47]. In order to assemble amino groups on the surface of nanoparticles, a layer of PEI was coated on the surface of nanoparticles by electrostatic adsorption to form OUCNPs@PEI. The Fourier Transform Infrared spectrum in Fig. S8(a) in the ESM was used to demonstrate the removal of oleic acid ligands and the successful coating of PEI on the surface of OUCNPs. The disappearance of the two bands at 2,924 and 2,853 cm^{-1} (corresponding to the asymmetric and symmetric stretching vibrations of methylene ($-CH_2$)), as well as the two bands at around 1,564 and 1,465 cm^{-1} (corresponding to the in-plane bending vibration of =C–H in the OA molecule) proved that the oleic acid ligand was successfully removed from the nanoparticle surface. The appearance of peaks at 2,827 and 2,934 cm^{-1} (corresponding to the shrinking vibrations of methylene stretching in the PEI molecule) indicates the successful formation of OUCNPs@PEI. The TEM image in Fig. S8(b) in the ESM demonstrates that the OUCNPs surface is successfully coated with a thin layer of PEI (about 1.98 nm) and the morphology of the OUCNPs@PEI does not drastically change. The OUCNPs@PEI still has a green emission under 980 nm laser excitation, indicating that the coating of PEI did not change the orthogonal excitation-emission property of OUCNPs (Fig. S8(c) in the ESM) [48].

Figure 4(b) shows the luminescence responses of OUCNPs@PEI to different concentrations of TNT under 980 nm excitation. The green light at 540 nm decreased more and more significantly with increasing TNT concentration. When the TNT concentration increased from 5 to 60 μM, the green fluorescence intensity of OUCNPs@PEI was linearly quenched, as shown in Fig. 4(c). The effect of fluorescence intensity on TNT concentration can be fitted by a linear regression equation (I = 14.0595 − 0.0604[TNT]) with a correlation value of 0.9959. The LOD (LOD = 3σ/K) value was calculated to be 3.04 μM. Compared to the already reported fluorescence detection of TNT (Table S2 in the ESM), our assay effect is relatively sensitive. While

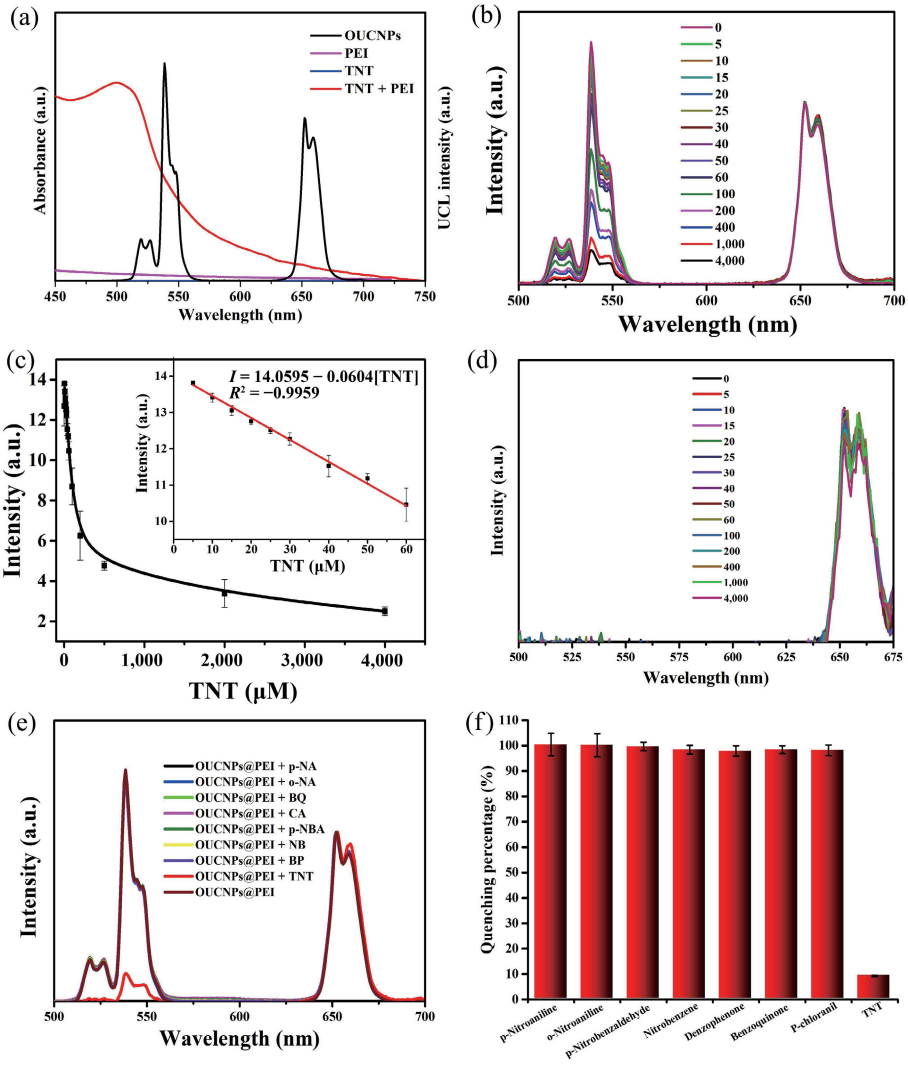

Figure 4 (a) The spectral overlap between the emission spectra of OUCNPs under 980 nm (0.5 W/cm²) excitation and absorption spectra of TNT, PEI, and TNT + PEI. (b) The luminescence spectra of OUCNPs@PEI after the addition of different concentrations of TNT (μM) at 980 nm (0.5 W/cm²) excitation. The luminescence intensity was normalized at 650 nm. (c) The fitted curves of luminescence intensity of OUCNPs@PEI after adding different concentrations of TNT (μM) under 980 nm (0.5 W/cm²) excitation. (d) The luminescence variations of OUCNPs@PEI under 808 nm (0.1 W/cm²) excitation after the addition of different amount of TNT (μM). (e) Under 980 nm (0.5 W/cm²) excitation, the luminescence variations of OUCNPs@PEI after the addition of same amount of p-NA, o-NA, BQ, CA, p-NBA, NB, BP, and TNT. (f) The corresponding percentage of luminescence quenching by adding different analytes.

at 808 nm excitation, the addition of TNT has almost no effect on the red emission at 650 nm (Fig. 4(d)), providing us with an internal reference signal for the assay, which helps to eliminate instrument and environmental noise interference and improve the accuracy of the assay.

Subsequently, to test the selectivity, we investigated the UV–visible absorption spectra of p-NA, o-NA, BQ, CA, p-NBA, NB, BP, and TNT (Fig. S9(a) in the ESM). The absorption spectra of these eight analytes when combined with PEI were then measured (Fig. S9(b) in the ESM). Only the PEI + TNT group showed a broad absorption around 500 nm. And then, the above eight analytes were detected separately using OUCNPs@PEI probe, and it was found that only the green emission of the TNT group was quenched, which was consistent with the measured absorption spectra (Fig. 4(e)). Calculations revealed that the green light dropped to less than 10% of its original value when the TNT concentration reached 4,000 μM (Fig. 4(f)). The above results further confirm that the as-designed OUCNPs@PEI probe had good selectivity to TNT.

In order to visualize the effect of TNT detection in a more practical way (Fig. 5), we made the TNT detection test strips by immersing the cut strips into OUCNPs@PEI aqueous solution for about 10 min to adsorb the OUCNPs@PEI into the filter paper due to hydrophilic and hydrogen bonding interactions, and then removed and placed in a dark place to dry naturally. Different concentrations of TNT acetonitrile solutions were dropped on the solid surface and then scraped with the test strips just prepared. The color of the test strips changed from green to yellow to red with increasing TNT concentration under 980 nm excitation. While under 808 nm, they showed red luminescence and no obvious difference in naked eye observation. These are consistent with the spectral changes in Fig. 4(b).

There is ample evidence that there will be a portion of residue on the hand when the hand intentionally or unintentionally touches an explosive such as TNT. Fingerprints carry information about a person's characteristics, so it is important for some occasions to visually detect TNT on-site and perform fingerprint imaging at the same time [49–51]. As a demonstration (Fig. 6(a)), fingerprints with different concentrations of TNT were collected on clean glass slides and then immersed in OUCNPs@PEI solution for about 10 min. Under 980 nm excitation, the fingerprints showed a transition from green to yellow to red with increasing TNT concentration (Fig. 6(b) and the upper part of Fig. 6(c)). It is worth noting that the fingerprint patterns obtained are relatively clear and sufficient for identification purposes. In contrast, under 808 nm excitation, the fingerprints are red with no concentration-dependent changes in color (lower part of Fig. 6(c)). However, the fingerprint pattern is not as clear as that obtained under 980 nm excitation, which is caused by the low power density of the 808 nm excitation used and the lack of obvious red light color rendering where the fingerprint traces are shallow. It is worth noting that in the actual TNT detection scenario, the aggregation of TNT powder causes particularly high TNT concentration in the local area, and it is easier to observe the very obvious color change under 980 nm irradiation. Therefore, the as-designed OUCNPs@PEI probe has good practical application value.

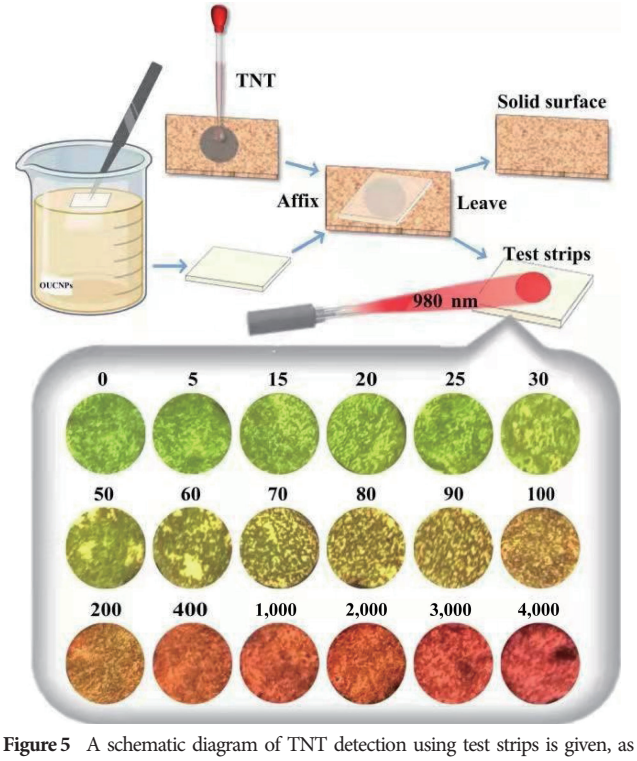

Figure 5 A schematic diagram of TNT detection using test strips is given, as well as corresponding photographs of test strips with different concentrations of TNT (μM) under 980 nm (0.5 W/cm^2) laser irradiation.

4 Conclusions

In conclusion, we designed and developed an OUCNPs (β-$NaErF_4$@$NaLuF_4$@$NaYF_4$:20%Yb, 2%Er@$NaLuF_4$) with relatively simple structure and high luminescence quality. Based on the property that $NaErF_4$@$NaLuF_4$ can emit near-monochromatic red UC emission under multi-wavelength excitations, $NaYF_4$:20%Yb, 2%Er and $NaLuF_4$ shells were epitaxially grown on its surface successively. By simply adjusting the thickness of the first inert shell $NaLuF_4$, the high-quality orthogonal luminescence properties of the designed OUCNPs were obtained: The fluorescence emission could be switched from red to green when the excitation wavelength was shifted from 808 to 980 nm. Compared with the reported OUCNPs, our unique features are (i) Nd^{3+}-free, (ii) no long-range energy migration between shell layers, (iii) two different excitation-emission modes are independent and do not interfere with each other. As a proof of concept, we demonstrated the application of the designed OUCNPs in anti-counterfeiting. We also prepared OUCNPs@PEI self-referencing fluorescent probes to achieve the quantification of TNT in solution with a detection limit of 3.04 μM. In addition the probe can be made into test strips for portable on-site visual TNT detection, or used to simultaneously image fingerprint patterns and detect explosive residues in fingerprints. The concept proposed in this work can be extended to the visual detection of a larger range of organic and biological molecules, and highlights the intelligent application of lanthanide materials.

Acknowledgements

This work was financially supported by the National Natural Science Foundation of China (Nos. 61875191, U2003127, 62171194, 11874355, and 21902057) and Natural Science Foundation of Jilin Province (No. 20210101380JC).

Electronic Supplementary Material: Supplementary material (some of the earlier reported OUCNPs (Table S1 in the ESM), comparison of the LOD of various fluorescent probes on TNT detection (Table S2 in the ESM), SEM image of $NaErF_4$ (Fig. S1 in the ESM), TEM image and corresponding size distribution of the OUCNPs (Fig. S2 in the ESM), schematic representation of the shell thickness of the OUCNPs (Fig. S3 in the ESM), XRD

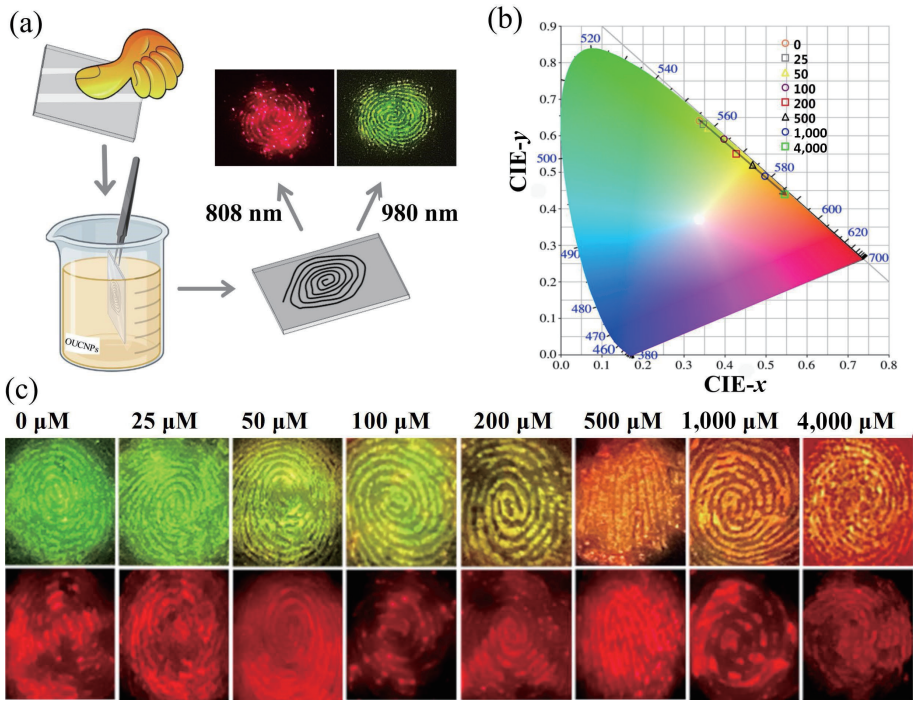

Figure 6 Visualized detection of the explosive TNT in the latent fingerprints. (a) Schematic diagram of the process of fingerprint acquisition and imaging. (b) CIE chromatic coordinates plotted from the emission spectra of OUCNPs@PEI when detecting different concentrations of TNT (μM) under 980 nm (0.5 W/cm^2) laser excitation. (c) The visual effects of TNT in latent fingerprint under 980 nm (0.5 W/cm^2) excitation and 808 nm (0.1 W/cm^2) excitation, respectively. The concentrations of TNT are 0, 25, 50, 100, 200, 500, 1,000, and 4,000 μM from left to right.

patterns of $NaErF_4$ and OUCNPs (Fig. S4 in the ESM), EDX spectrum of the OUCNPs (Fig. S5 in the ESM), emission spectra of OUCNPs under 1,530 nm excitation (Fig. S6 in the ESM), upconversion emission spectra of OUCNPs with different amounts of S1 ($NaLuF_4$) under 980 and 808 nm laser excitation, respectively (Fig. S7 in the ESM), FTIR spectra of OUCNPs-OA, OUCNPs@free, PEI, and OUCNPs@PEI, TEM image of the OUCNPs@PEI: emission spectra of OUCNPs@PEI under 808 and 980 nm excitation, respectively (Fig. S8 in the ESM), the UV-visible absorption spectra of TNT, BP, NB, p-NBA, CA, BQ, o-NA, p-NA, and the UV-visible absorption spectra of TNT, BP, NB, p-NBA, CA, BQ, o-NA, p-NA after addition of PEI (Fig. S9 in the ESM)) is available in the online version of this article at https://doi.org/10.1007/s12274-022-4693-8.

References

[1] Cheng, L.; Yang, K.; Zhang, S.; Shao, M. W.; Lee, S.; Liu, Z. Highly-sensitive multiplexed *in vivo* imaging using pegylated upconversion nanoparticles. *Nano Res.* **2010**, *3*, 722–732.

[2] Hong, A. R.; Kyhm, J. H.; Kang, G. M.; Jang, H. S. Orthogonal R/G/B upconversion luminescence-based full-color tunable upconversion nanophosphors for transparent displays. *Nano Lett.* **2021**, *21*, 4838–4844.

[3] Wang, M. ; Li, M. ; Yang, M. Y. ; Zhang, X. M. ; Yu, A. Y. ; Zhu, Y. ; Qiu, P. H. ; Mao, C. B. NIR-induced highly sensitive detection of latent fingermarks by $NaYF_4$: Yb, Er upconversion nanoparticles in a dry powder state. *Nano Res.* **2015**, *8*, 1800–1810.

[4] Zheng, K. Z.; Han, S. Y.; Zeng, X.; Wu, Y. M.; Song, S. Y.; Zhang, H. J.; Liu, X. G. Rewritable optical memory through high-registry orthogonal upconversion. *Adv. Mater.* **2018**, *30*, 1801726.

[5] Zhuang, Y. X. ; Chen, D. R. ; Chen, W. J. ; Zhang, W. X. ; Su, X. ; Deng, R. R. ; An, Z. F. ; Chen, H. M. ; Xie, R. J. X-ray-charged bright persistent luminescence in $NaYF_4$: Ln^{3+}@$NaYF_4$ nanoparticles for multidimensional optical information storage. *Light Sci. Appl.* **2021**, *10*, 132.

[6] Song, Y. P.; Lu, M. Y.; Mandl, G. A.; Xie, Y.; Sun, G. T.; Chen, J. B.; Liu, X.; Capobianco, J. A.; Sun, L. N. Energy migration control of multimodal emissions in an Er^{3+}-doped nanostructure for information encryption and deep-learning decoding. *Angew. Chem. , Int. Ed.* **2021**, *60*, 23790–23796.

[7] Ankenbruck, N.; Courtney, T.; Naro, Y.; Deiters, A. Optochemical control of biological processes in cells and animals. *Angew. Chem. , Int. Ed.* **2018**, *57*, 2768–2798.

[8] Zuo, M. Z.; Qian, W. R.; Xu, Z. Q.; Shao, W.; Hu, X. Y.; Zhang, D. M.; Jiang, J. L.; Sun, X. Q.; Wang, L. Y. Multiresponsive supramolecular theranostic nanoplatform based on Pillar[5]arene and diphenylboronic acid derivatives for integrated glucose sensing and insulin delivery. *Small* **2018**, *14*, 1801942.

[9] Wang, Z.; Qiu, X. E.; Xi, W. S.; Tang, M.; Liu, J. L.; Jiang, H.; Sun, L. N. Tailored upconversion nanomaterial: A hybrid nano fluorescent sensor for evaluating efficacy of lactate dehydrogenase inhibitors as anticancer drugs. *Sens. Actuator B Chem.* **2021**, *345*, 130417.

[10] Cui, S. S. ; Yin, D. Y. ; Chen, Y. Q. ; Di, Y. F. ; Chen, H. Y. ; Ma, Y. X. ; Achilefu, S. ; Gu, Y. Q. *In vivo* targeted deep-tissue photodynamic therapy based on near-infrared light triggered upconversion nanoconstruct. *ACS Nano*. **2013**, *7*, 676–688.

[11] Idris, N. M. ; Gnanasammandhan, M. K. ; Zhang, J. ; Ho, P. C. ; Mahendran, R. ; Zhang, Y. *In vivo* photodynamic therapy using upconversion nanoparticles as remote-controlled nanotransducers. *Nat. Med.* **2012**, *18*, 1580–1585.

[12] Ding, X.; Liu, J. H.; Liu, D. P.; Li, J. Q.; Wang, F.; Li, L. J.; Wang, Y. H.; Song, S. Y.; Zhang, H. J. Multifunctional core/satellite polydopamine@Nd^{3+}-sensitized upconversion nanocomposite: A single 808 nm near-infrared light-triggered theranostic platform for *in vivo* imaging-guided photothermal therapy. *Nano Res.* **2017**, *10*, 3434–3446.

[13] Carling, C. J.; Boyer, J. C.; Branda, N. R. Remote-control photoswitching using NIR light. *J. Am. Chem. Soc.* **2009**, *131*, 10838–10839.

[14] Di, Z. H.; Liu, B.; Zhao, J.; Gu, Z. J.; Zhao, Y. L.; Li, L. L. An orthogonally regulatable DNA nanodevice for spatiotemporally controlled biorecognition and tumor treatment. *Sci. Adv.* **2020**, *6*, eaba9381.

[15] Jayakumar, M. K. G.; Idris, N. M.; Zhang, Y. Remote activation of biomolecules in deep tissues using near-infrared-to-UV upconversion nanotransducers. *Proc. Natl. Acad. Sci. USA* **2012**, *109*, 8483–8488.

[16] Zhu, X. J.; Feng, W.; Chang, J.; Tan, Y. W.; Li, J. C.; Chen, M.; Sun, Y.; Li, F. Y. Temperature-feedback upconversion nanocomposite for accurate photothermal therapy at facile temperature. *Nat. Commun.* **2016**, *7*, 10437.
[17] Zheng, W.; Huang, P.; Tu, D. T.; Ma, E.; Zhu, H. M.; Chen, X. Y. Lanthanide-doped upconversion nano-bioprobes: Electronic structures, optical properties, and biodetection. *Chem. Soc. Rev.* **2015**, *44*, 1379–1415.
[18] Auzel, F. Upconversion and anti-stokes processes with f and d ions in solids. *Chem. Rev.* **2004**, *104*, 139–174.
[19] Bünzli, J. C. G. Lanthanide luminescence for biomedical analyses and imaging. *Chem. Rev.* **2010**, *110*, 2729–2755.
[20] Zhou, J.; Fan, X. X.; Wu, D.; Liu, J.; Zhang, Y. H.; Ye, Z. K.; Xue, D. W.; He, M. B.; Zhu, L.; Feng, Z. et al. Hot-band absorption of indocyanine green for advanced anti-stokes fluorescence bioimaging. *Light Sci. Appl.* **2021**, *10*, 182.
[21] Bünzli, J. C. G.; Piguet, C. Taking advantage of luminescent lanthanide ions. *Chem. Soc. Rev.* **2005**, *34*, 1048–1077.
[22] Chen, G. Y.; Qiu, H. L.; Prasad, P. N.; Chen, X. Y. Upconversion nanoparticles: Design, nanochemistry, and applications in theranostics. *Chem. Rev.* **2014**, *114*, 5161–5214.
[23] DaCosta, M. V.; Doughan, S.; Han, Y.; Krull, U. J. Lanthanide upconversion nanoparticles and applications in bioassays and bioimaging: A review. *Anal. Chim. Acta* **2014**, *832*, 1–33.
[24] Dong, H.; Sun, L. D.; Feng, W.; Gu, Y. Y.; Li, F. Y.; Yan, C. H. Versatile spectral and lifetime multiplexing nanoplatform with excitation orthogonalized upconversion luminescence. *ACS Nano.* **2017**, *11*, 3289–3297.
[25] Lai, J. P.; Zhang, Y. X.; Pasquale, N.; Lee, K. B. An upconversion nanoparticle with orthogonal emissions using dual NIR excitations for controlled two-way photoswitching. *Angew. Chem. , Int. Ed.* **2014**, *53*, 14419–14423.
[26] Li, X. M.; Guo, Z. Z.; Zhao, T. C.; Lu, Y.; Zhou, L.; Zhao, D. Y.; Zhang, F. Filtration shell mediated power density independent orthogonal excitations-emissions upconversion luminescence. *Angew. Chem. , Int. Ed.* **2016**, *55*, 2464–2469.
[27] Tang, M.; Zhu, X. H.; Zhang, Y. H.; Zhang, Z. P.; Zhang, Z. M.; Mei, Q. S.; Zhang, J.; Wu, M. H.; Liu, J. L.; Zhang, Y. Near-infrared excited orthogonal emissive upconversion nanoparticles for imaging-guided on-demand therapy. *ACS Nano.* **2019**, *13*, 10405–10418.
[28] Zhang, Z.; Jayakumar, M. K. G.; Shikha, S.; Zhang, Y.; Zheng, X.; Zhang, Y. Modularly assembled upconversion nanoparticles for orthogonally controlled cell imaging and drug delivery. *ACS Appl. Mater. Interfaces* **2020**, *12*, 12549–12556.
[29] Zuo, J.; Tu, L. P.; Li, Q. Q.; Feng, Y. S.; Que, I.; Zhang, Y. L.; Liu, X. M.; Xue, B.; Cruz, L. J.; Chang, Y. L. et al. Near infrared light sensitive ultraviolet-blue nanophotoswitch for imaging-guided "Off-On" therapy. *ACS Nano* **2018**, *12*, 3217–3225.
[30] Wang, L.; Dong, H.; Li, Y. N.; Liu, R.; Wang, Y. F.; Bisoyi, H. K.; Sun, L. D.; Yan, C. H.; Li, Q. Luminescence-driven reversible handedness inversion of self-organized helical superstructures enabled by a novel near-infrared light nanotransducer. *Adv. Mater.* **2015**, *27*, 2065–2069.
[31] Zuo, J.; Li, Q. Q.; Xue, B.; Li, C. X.; Chang, Y. L.; Zhang, Y. L.; Liu, X. M.; Tu, L. P.; Zhang, H.; Kong, X. G. Employing shells to eliminate concentration quenching in photonic upconversion nanostructure. *Nanoscale* **2017**, *9*, 7941–7946.
[32] Johnson, N. J. J.; Korinek, A.; Dong, C. H.; Van Veggel, F. C. J. M. Self-focusing by Ostwald ripening: A strategy for layer-by-layer epitaxial growth on upconverting nanocrystals. *J. Am. Chem. Soc.* **2012**, *134*, 11068–11071.
[33] Chen, Q. S.; Xie, X. J.; Huang, B. L.; Liang, L. L.; Han, S. Y.; Yi, Z. G.; Wang, Y.; Li, Y.; Fan, D. Y.; Huang, L. et al. Confining excitation energy in Er^{3+}-sensitized upconversion nanocrystals through Tm^{3+}-mediated transient energy trapping. *Angew. Chem. , Int. Ed.* **2017**, *56*, 7605–7609.
[34] Johnson, N. J. J.; He, S.; Diao, S.; Chan, E. M.; Dai, H. J.; Almutairi, A. Direct evidence for coupled surface and concentration quenching dynamics in lanthanide-doped nanocrystals. *J. Am. Chem. Soc.* **2017**, *139*, 3275–3282.
[35] Huang, J. S.; Yan, L.; Liu, S. B.; Song, N.; Zhang, Q. Y.; Zhou, B. Dynamic control of orthogonal upconversion in migratory core–shell nanostructure toward information security. *Adv. Funct. Mater.* **2021**, *31*, 2009796.
[36] Liu, X. W.; Wang, Y.; Li, X. Y.; Yi, Z. G.; Deng, R. R.; Liang, L. L.; Xie, X. J.; Loong, D. T. B.; Song, S. Y.; Fan, D. Y. et al. Binary temporal upconversion codes of Mn^{2+}-activated nanoparticles for multilevel anti-counterfeiting. *Nat. Commun.* **2017**, *8*, 899.
[37] Zhou, B.; Yan, L.; Huang, J. S.; Liu, X. L.; Tao, L. L.; Zhang, Q. Y. NIR II-responsive photon upconversion through energy migration in an ytterbium sublattice. *Nat. Photonics* **2020**, *14*, 760–766.
[38] Zhao, W. C.; Yang, X.; Feng, A. X.; Yan, X. L.; Wang, L. Q.; Liang, T.; Liu, J.; Ma, H. S.; Zhou, Y. Y. Distribution and migration characteristics of dinitrotoluene sulfonates (DNTs) in typical TNT production sites: Effects and health risk assessment. *J. Environ. Manage.* **2021**, *287*, 112342.
[39] Hu, Z. Y.; Jiang, N.; Zhang, Y. Q.; Xia, Y. Q.; Zhou, C. B. Propagation of shock wave and structure dynamic response of explosion in a subway station: A case study of Wuhan subway station. *J. Vibroeng.* **2020**, *22*, 1453–1469.
[40] Steinfeld, J. I.; Wormhoudt, J. Explosives detection: A challenge for physical chemistry. *Ann. Rev. Phys. Chem.* **1998**, *49*, 203–232.
[41] Yinon, J. Field detection and monitoring of explosives. *TrAC Trends Anal. Chem.* **2002**, *21*, 292–301.
[42] Jurado-Campos, N.; Chiluwal, U.; Eiceman, G. A. Improved selectivity for the determination of trinitrotoluene through reactive stage tandem ion mobility spectrometry and a quantitative measure of source-based suppression of ionization. *Talanta* **2021**, *226*, 121944.
[43] Baldin, M. N.; Bobrovnikov, S. M.; Vorozhtsov, A. B.; Gorlov, E. V.; Gruznov, V. M.; Zharkov, V. I.; Panchenko, Y. N.; Pryamov, M. V.; Sakovich, G. V. Effectiveness of combined laser and gas chromatographic remote detection of traces of explosives. *Atmos. Ocean. Opt.* **2019**, *32*, 227–233.
[44] Moazzen, S.; Zarei, A. R.; Mardi, K. Green sample preparation based on directly suspended droplet microextraction using deep eutectic solvent for ultra-trace quantification of nitroaromatic explosives by high performance liquid chromatography. *J. Anal. Chem.* **2021**, *76*, 1296–1304.
[45] Zhang, K.; Zhou, H. B.; Mei, Q. S.; Wang, S. H.; Guan, G. J.; Liu, R. Y.; Zhang, J.; Zhang, Z. P. Instant visual detection of trinitrotoluene particulates on various surfaces by ratiometric fluorescence of dual-emission quantum dots hybrid. *J. Am. Chem. Soc.* **2011**, *133*, 8424–8427.
[46] Lei, Z. D.; Ling, X.; Mei, Q. S.; Fu, S.; Zhang, J.; Zhang, Y. An excitation navigating energy migration of lanthanide ions in upconversion nanoparticles. *Adv. Mater.* **2020**, *32*, 1906225.
[47] Bogdan, N.; Vetrone, F.; Ozin, G. A.; Capobianco, J. A. Synthesis of ligand-free colloidally stable water dispersible brightly luminescent lanthanide-doped upconverting nanoparticles. *Nano Lett.* **2011**, *11*, 835–840.
[48] Feng, Y. S.; Li, Z.; Li, Q. Q.; Yuan, J.; Tu, L. P.; Ning, L. X.; Zhang, H. Internal OH^- induced cascade quenching of upconversion luminescence in $NaYF_4$: Yb/Er nanocrystals. *Light Sci. Appl.* **2021**, *10*, 105.
[49] Lai, F. L.; Wang, Y.; Li, D. D.; Sun, X. S.; Peng, J.; Zhang, X. D.; Tian, Y. P.; Liu, T. X. Visible light-driven superoxide generation by conjugated polymers for organic synthesis. *Nano Res.* **2018**, *11*, 1099–1108.
[50] Wang, M. Latent fingermarks light up: Facile development of latent fingermarks using NIR-responsive upconversion fluorescent nanocrystals. *RSC Adv.* **2016**, *6*, 36264–36268.
[51] Wang, M.; Li, M.; Yu, A. Y.; Zhu, Y.; Yang, M. Y.; Mao, C. B. Fluorescent nanomaterials for the development of latent fingerprints in forensic sciences. *Adv. Funct. Mater.* **2017**, *27*, 1606243.